

# Quasi-static fault growth and shear fracture energy in granite

D. A. Lockner\*, J. D. Byerlee\*, V. Kuksenko†, A. Ponomarev‡ & A. Sidorin‡

\* US Geological Survey, 345 Middlefield Road, Menlo Park, California 94025, USA

† A. F. Ioffe Physical-Technical Institute, USSR Academy of Sciences, Polytechnicheskaya 26, Leningrad, USSR 194021

‡ Institute of Physics of the Earth, USSR Academy of Sciences, Bolshaya Gruzinskaya 10, Moscow D-242, USSR 123810

The failure process in a brittle granite sample can be stabilized by controlling axial stress to maintain a constant rate of acoustic emission. As a result, the post-failure stress curve can be followed quasi-statically, extending to hours the fault growth process which normally would occur violently in a fraction of a second. Using a procedure originally developed to locate earthquakes, acoustic emission arrival-time data are inverted to obtain three-dimensional locations of microseisms. These locations provide a detailed view of fracture nucleation and growth.

EXPERIMENTAL studies of the fracture of brittle rock have been made difficult by the tendency for fault growth to proceed in a violent, uncontrolled manner after fault initiation. Past attempts to stabilize the failure process have concentrated on the development of 'stiff' loading frames which store relatively little elastic energy during the loading cycle<sup>1-3</sup>. But many rocks store sufficient elastic energy to drive unstable faulting on their own, so fracture stabilization requires the loading system to remove energy dynamically during the failure process<sup>4</sup>. To accomplish this task, we have developed a fast-acting axial control system that adjusts the load applied to the sample to maintain a constant acoustic-emission rate. We are therefore able to study the post-peak-stress region, in which a macroscopic fault forms in the sample, under quasi-static conditions. We have also recorded relative arrival times and amplitudes of acoustic-emission signals occurring in the sample as it is deformed. Inversion of the arrival-time data provides three-dimensional locations of acoustic-emission hypocentres, resulting in detailed imaging of fracture nucleation and propagation. In addition, we have analysed amplitude information to provide estimates of fracture energy and other fault propagation parameters.

## Experimental procedure

A right cylinder of intact Westerly granite was precision ground to a length of 190.5 mm and a diameter of 76.2 mm and jacketed in a polyurethane tube. Six piezoelectric transducers (resonance at 0.6 MHz) were attached directly to the rock and used to monitor the high-frequency acoustic emission generated in the sample as it was stressed. Four other transducers were used to measure periodically the P-wave (compressional wave) velocity field during the experiment. The sample was deformed in a triaxial apparatus at a constant confining pressure  $P_c$  of  $50.0 \pm 0.2$  MPa. The axial load was applied to the sample with a hydraulic ram controlled by a fast-acting valve and was automatically adjusted to maintain an approximately constant acoustic-emission rate. This required reversing the ram during fracture growth. Axial displacement was measured outside the pressure vessel and circumferential strain was measured with a foil strain gauge attached to the mid-plane of the sample.

Acoustic emission signals were amplified and sent to a six-

channel monitoring system which recorded on digital tape the relative P-wave arrival times at the transducer sites (to  $\pm 0.05 \mu\text{s}$ ), as well as amplitude and first-motion information. The arrival-time data were later inverted to provide three-dimensional locations for the source events, presumably impulsive microcracking events, that emitted the acoustic signals. The recording system and analysis techniques are discussed elsewhere<sup>5,6</sup>. Arrival-time precision of the monitoring system sets a limit of  $\pm 0.3$  mm for the accuracy of determining source locations. In practice, however, other measurement errors further degrade the location accuracies. The primary source of error is a tendency to pick systematically late arrivals for low-amplitude, emergent waveforms<sup>7</sup>. We estimate that location uncertainties for the large-amplitude acoustic-emission events used in this analysis are typically  $\pm 3$  mm. This error estimate is supported by the tight clustering of acoustic-emission locations shown in Fig. 2. To aid in the event location analysis, the average P-wave velocity field<sup>8</sup> was determined independently during the course of the experiment by periodically measuring transit times of artificially generated acoustic pulses travelling along three different ray paths in the sample.

## Fault development inferred from AE locations

In Fig. 1, axial stress is plotted as a function of axial displacement. Fault nucleation occurred soon after peak stress, where there was an abrupt reversal in slope. Figure 2 shows locations of acoustic emissions in six sequential time intervals that correspond to the stress intervals indicated in Fig. 1. Events occurring in each time interval in Fig. 2 are shown in two projections. In the upper plot of each pair, the sample is viewed along-strike, so that the  $\sim 68^\circ$  dip of the developing fault plane is clearly seen. In the lower plot, the sample has been rotated clockwise by  $90^\circ$  (as viewed from the top) so that the fault plane is seen face-on. Figure 2a shows the relatively diffuse acoustic emission

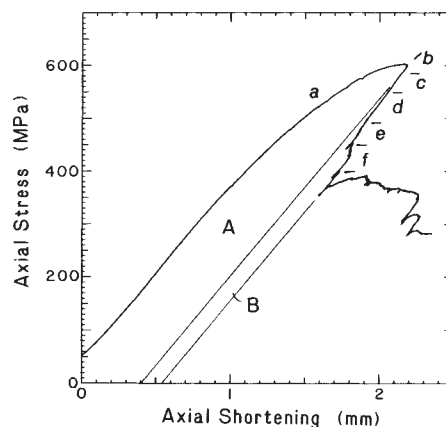


FIG. 1 Axial stress plotted against axial displacement for Westerly granite at  $P_c = 50$  MPa. Letters along curve correspond to plots shown in Fig. 2. Region A represents non-recoverable work expended in deforming sample to the point of fault nucleation; region B is work expended during initial fault growth.

that occurs during loading through peak stress. In Fig. 2b, the first 150 s of fault nucleation are plotted, showing that the fault has already established its position and inclined orientation, even though it is only about 20 mm across. The nucleation zone of  $\sim 2,000 \text{ mm}^3$  rapidly evolves into the nascent fault, narrowing into a half-penny shape that defines the position and orientation of the fracture. Notice that the fracture nucleated at the sample surface; this was the case for all three granite samples tested so far. In Figs 2c–f, the fracture gradually propagates across the sample as a well-defined band of activity. Relative quiescence in the wake of the advancing fracture front suggests that the band of activity represents a process zone as modelled by Rice<sup>9,10</sup>. This process zone is 20–30 mm wide in the direction of propagation. Examination in thin section shows that the thickness of the process zone, normal to the fracture surface, is 2–5 mm. Although the fracture grows unimpeded to the upper corner of the sample, it unfortunately propagates downward into the lower steel endplug. As a result, even at the end of the experiment an unbroken column of rock supports part of the axial load. Thus, the sample strength never drops to the frictional sliding strength of  $\sim 190 \text{ MPa}$ . Although the final stage of fault growth is complicated by the interference of the lower endplug, we infer that nucleation and early growth are little affected. Nucleation occurs near the sample mid-plane, far from the end effects produced by a mismatch in modulus between rock and steel.

### Variations in $b$

The frequency–magnitude relation for earthquakes is commonly described in terms of  $b$ , defined by  $\log N = a - bM$  where  $N$  is number of earthquakes larger than magnitude  $M$  and  $a$  and  $b$  are constants. Analyses of earthquake foreshocks<sup>11,12</sup> have revealed precursory variations in  $b$ . This relation has also been applied in the laboratory to studies of acoustic emission where, for example,  $b$  has been calculated for loading of both intact samples<sup>13</sup> and samples containing faults<sup>14</sup>. By assuming that the stress intensity factor at active crack tips would increase as a rock approaches failure, Main and Meredith developed a model

that predicts a drop in  $b$  in the pre-failure region followed by a recovery after faulting. They observed this decrease and recovery of  $b$  during deformation of porous sandstone. Weeks *et al.*<sup>14</sup> reported similar behaviour for the amplitude of acoustic emission preceding stick-slip on a pre-existing fault in granite.

Because we recorded the amplitudes of the acoustic emission, we can look for variations in  $b$ . For each event that triggered the acquisition system, the amplitude of the first peak of the incoming wave train was recorded for each transducer. Amplitudes were then adjusted for  $1/r$  geometric spreading and averaged over the six transducers to give an equivalent event amplitude  $A$  at a distance of 10 mm from the hypocentre. This is only an estimate of the true event amplitude because it depends on averaging over six directions the effects due to radiation pattern, transducer incidence angle, attenuation and other properties. Referred to input signal level, the acquisition system has a dynamic range of 0.8–17.8 mV which corresponds to a range in  $A$  of  $\sim 5$ –120 mV. To analyse variations in  $b$ , we have used events occurring in a volume of rock in the shape of a 20-mm-thick disk taken from the central region of the sample. By restricting ourselves to events in this region, we minimize biases due to, for example, attenuation. We assume that  $M \propto \log A$ , so that  $b$  is the slope of the plot of  $\log N$  against  $\log A$ . Representative plots for pre-nucleation, nucleation and propagation events are shown in Fig. 3a. The temporal variation of  $b$  is plotted in Fig. 3b. In agreement with Main and Meredith<sup>13</sup>,  $b$  decreases to a minimum at the time of fault nucleation. Then, during the propagation phase,  $b$  recovers to over 50% of its initial value.

### Energy balance and related parameters

In this section we estimate the acoustic energy radiated during fracture propagation. Combining these data with stress and displacement measurements allows us to examine the local energy release rate during fracturing. To calculate acoustic energy we assume that the radiated acoustic-emission energy  $E_{AE}$  is proportional to  $A^2$  and also that  $E_{AE} \propto E_{in}$  where  $E_{in}$  is dissipative, inelastic energy consumed during deformation of

FIG. 2 Sequential plots of locations of acoustic emission. Stress interval for each plot is shown in Fig. 1. Upper plots show events viewed along-strike of eventual fault plane (seen as diagonal band of events). Lower plots show same events when fault plane is viewed face-on. Fault nucleates in  $b$  and propagates across sample in  $c$ – $f$ . A distinct fracture front develops, in  $d$ – $f$ , as fault grows. Number of events per plot in  $a$ – $f$  are 474, 123, 402, 1088, 2292 and 4038, respectively.

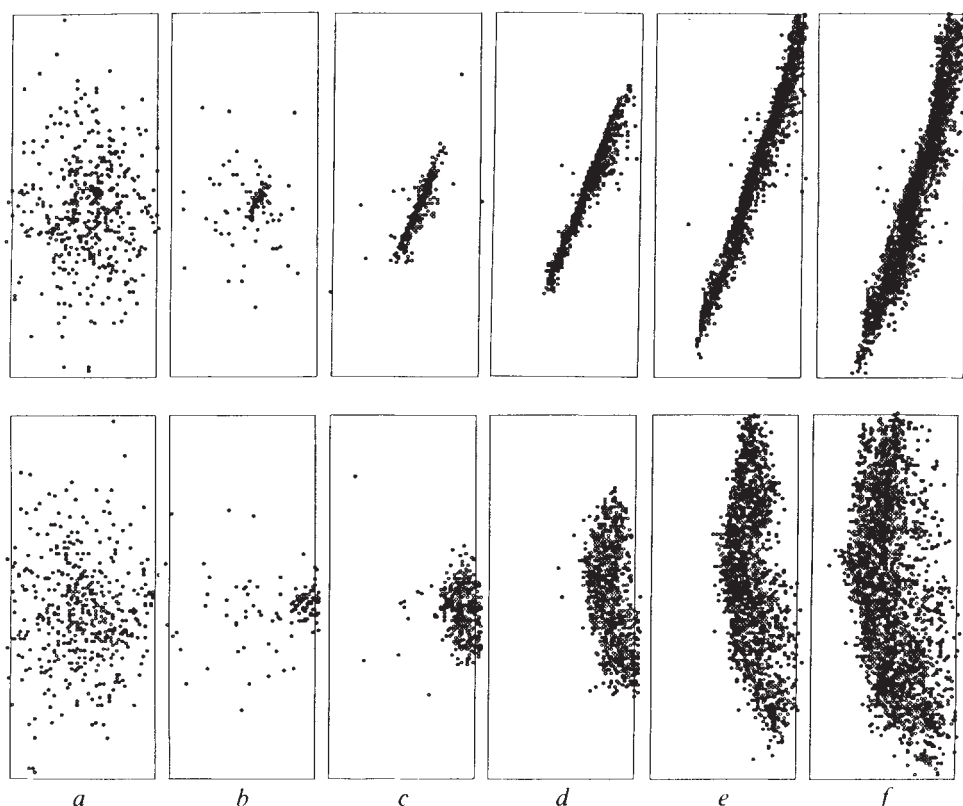
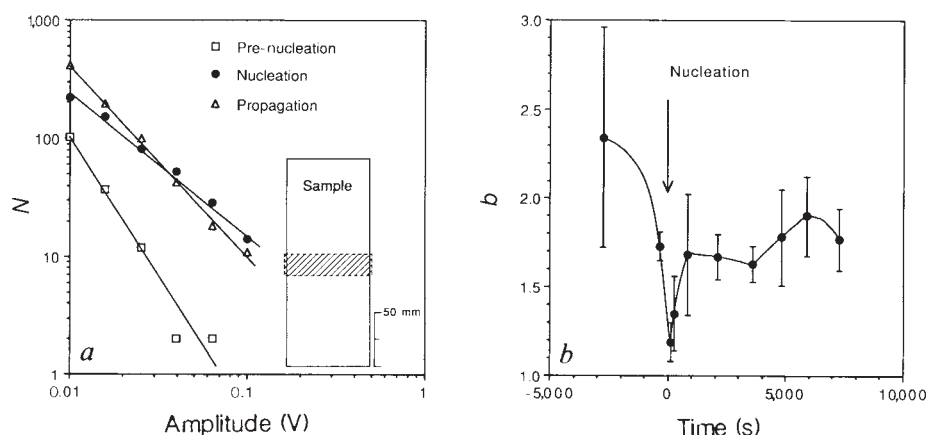


FIG. 3 *a*, Representative amplitude-frequency plots used to determine  $b$ . Insert shows region sampled in determining  $b$ -value. *b*, Plot of variation of  $b$  during experiment with  $2\sigma$  error bars. Minimum occurs during fault nucleation phase.



the sample. These relations yield  $E_{in} = kA^2$  where  $k$  is a scaling parameter. Ideally, the transducers would be calibrated so that amplitude would express, for example, displacement. Because we do not know the response function for the transducers, we express their output in volts and include the necessary scaling factor in  $k$ . The transducers have a resonance at 0.6 MHz and should be most sensitive to wavelengths of a few millimetres. To the degree that the frequency-amplitude relation is stable, however, the frequency dependence of  $k$  will not change. This assumption will be tested in future experiments. In addition to transducer response characteristics,  $k$  also includes the acoustic efficiency of the inelastic deformation in the rock. To determine  $k$ , we calculate  $\int dE_{in}$  and  $\sum A^2$  for a portion of the experiment. Inelastic work is calculated in two parts:  $\int dE_{in} = \int F_a dl_{in} + \int F_r dr_{in}$ . The axial force  $F_a$  is  $\sigma_a \times$  area of end of sample and the radial force  $F_r$  is  $P_c \times$  area under jacket;  $dl_{in}$  is calculated from the record of axial displacement by removing elastic shortening;  $dr_{in}$  is calculated from the record of circumferential strain gauge (not shown). Once the fracture nucleates, deformation becomes inhomogeneous. This will not affect the calculation of axial work because total axial force and displacement are measured. By contrast, the strain gauge provides a local measurement and cannot give the total work expended against the confining medium. The strain-gauge signal is, however, the only information available for the lateral strain. Using the strain-gauge output at face value, the confining pressure provides less than 30% of the total energy flux during fault growth so that the errors due to strain inhomogeneity are not expected to affect the basic results.

Two determinations of  $k$  were made using events from pre-nucleation and post-nucleation portions of the experiment (shown as regions A and B in Fig. 1). The post-nucleation determination included fault growth up to the point where the fault ran into the lower endplug. Pre- and post-nucleation calibrations were  $3,300 \pm 550$  and  $46 \pm 8 \text{ J V}^{-2}$ , respectively. The difference of a factor of 70 in the calibrations is larger than the numerical uncertainties in the calculations and indicates a sig-

nificant increase in efficiency of high-frequency acoustic energy generated during fracture propagation. This increase in efficiency following fault initiation is consistent with the observed decrease in  $b$ . A decrease in  $b$  will result in proportionately fewer low-amplitude events. As the acquisition system does not detect events below the pre-set threshold level (0.8 mV), a decrease in  $b$  corresponds to a decrease in the fraction of acoustic energy undetected by the system. Other effects<sup>10</sup>, such as a change in the relative amounts of slow, subcritical microcrack growth and rapid, unstable microcracking, may also contribute to the change in calibration.

The lack of detected activity following the passage of the fracture front (Fig. 2*d-f*) may also affect our determination of acoustic efficiency. The decrease of acoustic emission from the newly formed fault surface may be related to the reduction in grain size that occurs as the fracture front passes. These smaller grains should produce acoustic emission with a different frequency content from the unfractured rock and should therefore be detected with a different efficiency by the transducers used. In related experiments we have had no difficulty in detecting acoustic emission from slip on existing faults<sup>14,15</sup>, suggesting that this effect does not introduce a significant bias. This issue should be clarified in experiments which will be extended to include slip on the fully developed fault.

We can now examine the energy release rate for shear fracturing. Following Rice<sup>9,10</sup>, we define the breakdown zone at the advancing fracture tip as the region over which shear stress drops from its peak value  $\tau_p$  to the frictional sliding strength  $\tau_f$  (Fig. 4). We denote the in-plane width of this zone by  $w$  and the total displacement by  $\delta^*$ . The energy release rate  $G$  (Fig. 4) as used in fracture mechanics<sup>3,9,10</sup>, is the excess, above the frictional energy  $E_f$ , expended in the process zone. We first calculate the total energy release rate, denoted by  $G_t = E_f + G$ , by analysing the radiated acoustic energy and using the post-nucleation calibration of acoustic-emission amplitudes.

In Fig. 5*a* we show time plots of the cumulative acoustic energy  $A^2$  from sources within unit cubes 10 mm on a side. Cube

FIG. 4 Schematic diagram showing slip weakening of rock in process zone. Total energy release rate  $G_t = E_f + G$ .

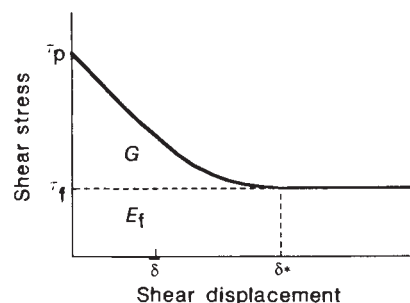
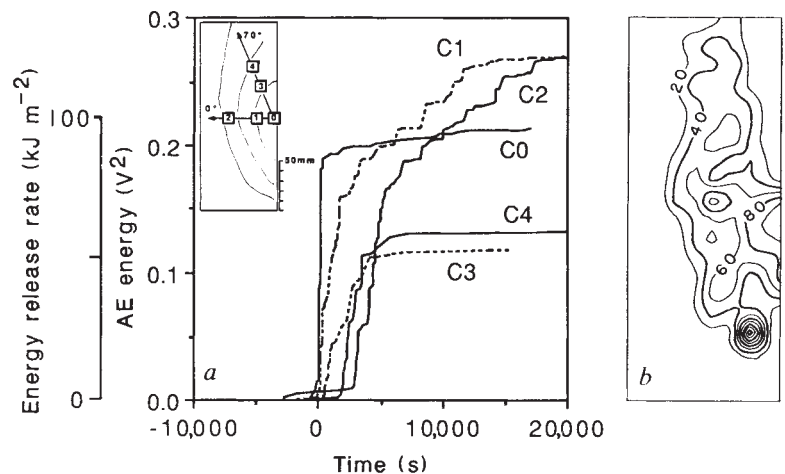




FIG. 5 a, Time plots of cumulative acoustic energy. Calibration of acoustic energy provides estimate of local energy release rate  $G_t$ . b, Distribution of  $G_t$  on fault surface after 7,000 s of fault growth. Contour intervals are  $20 \text{ kJ m}^{-2}$ . Variation in energy release indicates local strength heterogeneity.



CO is centred in the nucleation zone. Given the geometry of the fault, cubes C1 and C2 sample pure mode-III anti-plane growth. Cubes C3 and C4 lie along a line inclined  $70^\circ$  to the horizontal. Along this direction the relative contributions of mode-II in-plane and mode-III anti-plane shear are approximately 3 to 1. All samplings show a rapid rise in acoustic energy, marking the arrival of the fracture front, followed by a gradual decrease in the level of acoustic activity. Figure 5a shows a correlation between total radiated acoustic energy and propagation direction. Expressed in terms of total energy release rate, we find  $G_t^{\text{III}}/G_t^{\text{II}} \approx 2$ . The apparent difference in  $G_t$  in the two propagation directions can be checked in the following way. In Fig. 5b we plot the total energy release ( $\text{kJ m}^{-2}$  per unit area) in the 7,000-s interval following nucleation. At this time, the fracture front has traversed slightly more than halfway across the sample. Although care was taken to choose a uniform, fine-grained (0.2-mm-diameter) sample, the energy release pattern shows distinct local structure which indicates significant strength heterogeneity. Detailed examination of the sequence of acoustic locations shows that fault growth was indeed episodic, as if strong patches periodically retarded local fault growth. The pattern in Fig. 5b shows a generally lower energy release rate in the upper portion of the sample than in the central region. Although this may be related to the direction of fault propagation, it could also be the result of a pre-existing strength heterogeneity. The fault plane did propagate more rapidly into the upper sample region, indicating that this area was relatively easy to fracture. Future experiments should help to clarify this question. Evaluation of the acoustic energy release after 10,000 s gives an average release rate of  $G_t \approx 9 \times 10^4 \text{ J m}^{-2}$  with local variation of up to 50%.

Wong<sup>3</sup> and Rice<sup>9</sup> calculated the excess energy release rate  $G$  from a plot of shear stress against displacement such as that shown in Fig. 4. In our experiment, however,  $G_t$  is probably the more appropriate parameter to consider, because there is no pre-existing fault to which frictional energy  $E_f$  can be related.

We will, however, briefly indicate how to modify our results to estimate  $G$ . By performing the same calculation as Rice and Wong, we can obtain a rough estimate of  $G$  from our experiment. The result is  $G = 1.3 \times 10^4 \text{ J m}^{-2}$ , in agreement with their range of estimates,  $(0.3-7.3) \times 10^4 \text{ J m}^{-2}$ . Our estimate of  $G$  is based solely on average stress and displacement measurements, but as our sample is larger than the process zone, this calculation is not strictly correct.

To estimate  $G$  from our local acoustic energy determinations, we need to determine the local frictional energy  $E_f$  expended during fault formation. This requires knowledge of  $\tau_f$  and  $\delta^*$  (Fig. 4) occurring on the fault as the process zone moves by.  $\tau_f$  is known from related experiments and  $\delta^*$  can be estimated from  $^{10} w \approx (2 \text{ to } 3) \mu \delta / (\tau_p - \tau_f)$  where  $w$  is the width of the process zone,  $\mu$  is the shear modulus, and  $\delta \approx \delta^*/2$  is the 'characteristic' breakdown slip. Using reasonable values for the parameters results in  $E_f = (0.8 \pm 0.3) \times 10^4 \text{ J m}^{-2}$ . Because  $G = G_t - E_f$ , we conclude that within the resolution of this experiment,  $G = (8 \pm 5) \times 10^4 \text{ J m}^{-2}$  and  $G_t = (9 \pm 5) \times 10^4 \text{ J m}^{-2}$  with a significant portion of the uncertainties related to either local strength heterogeneity or direction of fracture propagation.

By controlling stress to maintain a constant rate of acoustic emission, we have stabilized the failure process in brittle rock. Combined with arrival times and amplitudes of the acoustic-emission signals, this technique can provide a detailed view of fault nucleation and growth. This approach to the study of fault growth opens a number of possibilities for future research in such areas as earthquake dynamics and earthquake prediction. In future experiments we plan to investigate the roles of rock heterogeneity, flaw size and fluid pressure on the nucleation process. This should increase our understanding of the transient phenomena that occur before earthquake rupture. In addition, a more sophisticated treatment of the acoustic-amplitude data should provide new methods for determining the local energetics of fault propagation including energy release associated with strength barriers and propagation direction. □

Received 25 October 1990; accepted 16 January 1991.

1. Wawersik, W. R. & Fairhurst, C. *Int. J. Rock Mech. Mining Sci.* **7**, 561-575 (1970).
2. Wawersik, W. R. & Brace, W. F. *Rock Mech.* **3**, 61-85 (1971).
3. Wong, T. F. *J. geophys. Res.* **87**, 990-1000 (1982).
4. Terrada, M., Yanagidani, T. & Ehara, S. in *Proc. 3rd Conf. on Acoustic Emission/Microseismic Activity in Geol. Structures and Materials* (eds Hardy, H. R. & Leighton, F. W.) 159-171 (Trans-Technical, Clausthal-Zellerfeld, 1984).
5. Lockner, D. A. & Byerlee, J. D. in *Proc. 2nd Conf. on Acoustic Emission/Microseismic Activity in Geol. Structures and Materials* (eds Hardy, H. R. & Leighton, F. W.) 11-25 (Trans-Technical, Clausthal-Zellerfeld, 1980).
6. Lockner, D. A., Byerlee, J. D., Kukensko, V., Ponomarev, A. & Sidorin, A. *Fault Mechanics and Transport Properties of Rocks* (eds Evans, B. & Wong, T.-F.) (Academic, London, in the press).

7. Lockner, D. A. & Byerlee, J. D. *Pure appl. Geophys.* **116**, 765-772 (1978).
8. Lockner, D. A., Walsh, J. B. & Byerlee, J. D. *J. geophys. Res.* **82**, 5374-5378 (1977).
9. Rice, J. R. in *Physics of the Earth's Interior* (eds Dziewonski, A. M. & Boschi, E.) (Italian Physical Society and North-Holland, Amsterdam, 1980).
10. Rice, J. R. in *Proc. 1st Int. Congress on Rockbursts and Seismicity in Mines, Johannesburg 1982* (eds Gay, N. C. & Wainwright, E. H.) 57-62 (Symp. Ser. No. 6, South African Institute of Mining and Metallurgy, Johannesburg, 1984).
11. Von Seggern, D. *Geophys. Res. Lett.* **7**, 637-640 (1980).
12. Jin, A. & Aki, K. *J. geophys. Res.* **91**, 665-673 (1986).
13. Main, I. G. & Meredith, P. G. *Tectonophysics* **167**, 273-283 (1989).
14. Weeks, J. D., Lockner, D. A. & Byerlee, J. D. *Bull. seism. Soc. Am.* **68**, 333-341 (1978).
15. Lockner, D. A. & Byerlee, J. D. *J. geophys. Res.* **82**, 2018-2026 (1977).